**PAPER • OPEN ACCESS**

# Computational study of oxide stoichiometry and variability in the Al/AlOx/Al tunnel junction

To cite this article: Paul Lapham and Vihar P Georgiev 2022 *Nanotechnology* **33** 265201

View the article online for updates and enhancements.

# Computational study of oxide stoichiometry and variability in the Al/AlOx/Al tunnel junction

## Paul Lapham and Vihar P Georgiev

Device Modelling Group, James Watt School of Engineering, University of Glasgow, Glasgow G12 8QQ, United Kingdom

E-mail: Vihar.Georgiev@glasgow.ac.uk

CrossMark

## Abstract

Aluminium tunnel junctions are key components of a wide variety of electronic devices. These superconducting tunnel junctions, known as Josephson Junctions (JJ's) are one of the main components of superconducting qubits, a favourite qubit technology in the race for working quantum computers. In this simulation study our JJ configurations are modelled as two aluminium electrodes which are separated by a thin layer of amorphous aluminium oxide. There is limited understanding of how the structure of the amorphous oxide barrier affects the performance and shortcomings of JJ systems. In this paper we present a computational study which combines molecular dynamics, atomistic semi-empirical methods (Density Functional Tight Binding) and non-equilibrium Green's function to study the electronic structure and current flow of these junction devices. Our results suggest that the atomic nature of the amorphous barrier linked to aluminum-oxygen coordination sensitively affects the current–voltage ($IV$) characteristics, resistance and critical current. Oxide stoichiometry is an important parameter that can lead to variation in resistance and critical currents of several orders of magnitude. The simulations further illustrate the variability that arises due to small differences in atomic structure across amorphous barriers with the same stoichiometry, density and barrier length. Our results also confirm that the charge transport through the barrier is dominated by metallic conduction pathways.

Keywords: DFTB, NEGF, quantum computing, qubits, Josephson junctions, material modelling, simulation

(Some figures may appear in colour only in the online journal)

## 1. Introduction

Josephson junctions (JJ's) are superconducting tunnel junctions that consist of two superconductors separated by a thin insulating layer. They are key to several different device technologies, notably SQUIDs and superconducting qubits [1, 2]. With the race to quantum supremacy well underway, superconducting qubits are a favourite among many qubit technologies [3]. JJ are key to the superconducting qubit as it creates non-linearity in an otherwise harmonic potential [4]. One of the main challenges faced in quantum computing is decoherence of qubits. Until now, most improvements to decoherence times has been achieved through circuit design and engineering. The thin oxide insulating barrier in typical JJ devices is amorphous and considered to be one of the main sources of noise and decoherence in qubits, due to two level defects within the barrier [5, 6]. In addition, the amorphous nature of the barrier leads to variability in junction performance and poor control of the critical current, $I_c$, a key

parameter which affects the qubit energy levels and operating frequencies [7]. Although in wide use experimentally and the physics has been understood since the 1960s, there is still a poor fundamental understanding from an atomic perspective of how the structure of the junction affects the performance and variability of the device and subsequently qubit applications [8, 9].

Computational modelling is an efficient tool to study the atomic structure of materials and their electron transport. Experimental exploration of junctions is expensive, painstaking and very time consuming [10–12]. Through the use of modelling, we can create, probe and study different junction types, properties and effects more easily. Accurate and efficient computational models can improve understanding and help the fabrication and design of JJ's for qubit and other applications. In combining classical molecular dynamics to create the amorphous barrier, Density Functional Tight Binding (DFTB) model to study the electronic structure with non-equilibrium Green's function (NEGF) to study the transport in three dimensions. We can efficiently and accurately study JJ's and gain a fundamental understanding of how their material properties influence their operation.

The archetypal Josephson Junction is the Al/AlOx/Al junction, it is the most studied and is the focus of this paper. There are several challenges in modelling the Al/AlOx/Al system computationally, hence there are relatively few studies in the literature. Firstly, the size of realistic junctions for qubits are 100 nm × 100 nm (and can range to several $\mu m^2$), these dimensions are very computationally demanding for atomistic simulations, such as DFTB model. Applying periodic boundary conditions can alleviate some of these issues but not all. Secondly, the oxide is usually grown, but current Molecular Dynamics methods cannot simulate experimental timescales or pressures. Growth simulations are possible but cumbersome and no guarantee that the amorphous nature of the structure is realistic. Lastly, the amorphous barrier itself, is subject to significant debate in terms of structure, electronic properties and oxide stoichiometry [13–15]. Though crystalline aluminium oxide is $Al_2O_3$ (or $AlO_{1.5}$), experimental evidence suggests the barrier in Al/AlOx/Al is in fact oxygen deficient and has a stoichiometry that ranges from 0.8 to 1.3, with typical values of 1.1 in regular junctions [16]. It has been shown that barrier stoichiometry has a sensitive effect on the atomic and electronic structure of the barrier which significantly alters the transport properties and thus device performance [17]. We aim to explore this further through simulation of junctions with different oxide stoichiometries using atomistic semi-emipirical simulation methodology.

In this work, we study several Al/AlOx/Al tunnel junctions computationally using DFTB/NEGF simulations. Our aim is to probe how the stoichiometry (Al:O ratio) of the barrier influences the atomic structure, normal state resistance and the resulting charge transport through the oxide barrier. Through resistance, we can link the normal state conduction to the superconducting current, and gain an insight to how the stoichiometry influences the $I_c$. Using simulation we probe sources of variability within the junction. We also aim to understand transmission pathways in the barrier and how it relates to the amorphous structure of the barrier.

## 2. Simulation methodology

### 2.1. Electronic structure calculations with DFTB

Density Functional based Tight Binding (DFTB) method is an approximate method which is based and parameterised from Density Functional Theory (DFT). In this method, an optimized atomic orbital minimal basis set is used and the Kohn–Sham potential is approximated from a two center approximation. The overlap matrix is given by pre-calculated pairwise integrals between different basis functions these are stored in so called Slater–Koster tables. The density matrix is calculated self consistently. Due to the pre-calculated overlap matrix, this method is computationally efficient whilst maintaining a high level of accuracy comparable to DFT.

Although DFTB is a semi-empirical method parameterized for certain systems using Density Functional Theory, it has been shown to be transferable and suggests it can describe with reasonable accuracy the important physics of the systems whilst significantly reducing computational costs [18]. For a comprehensive description of DFTB and its implementation readers are directed to the cited literature [18–20]. Also in this simulation study we are emphasising the difference between different barrier configurations, as long as as all the simulations are performed with identical computational set up, our inferences based on structure effects should be valid.

### 2.2. Creating the junctions using molecular dynamics

It is very important to ensure the barrier is indeed amorphous. Whilst, it is possible to grow structures through Molecular Dynamics, replicating experimental times and pressures is still beyond the computational capabilities. Therefore, we have elected a more efficient approximation here through simulated annealing method. This method has been successfully applied to create realistic amorphous structures, including $Al_2O_3$ [21, 22].

Starting from a $3 \times 3 \times 1$ slab of Corundum, we adjust the $z$ coordinate of the simulation box, to ensure the reduced density seen experimentally for amorphous AlOx is replicated, 3.18 g cm$^{-3}$, which is 0.8 times the density of Corundum (3.97 g cm$^{-3}$). Oxygen atoms are manually removed to create the desired stoichiometry for the sample. The $z$ coordinate is adjusted relative to the change in mass from the stoichiometry to ensure a density of 3.18 g cm$^{-3}$ for all samples to be comparable. An NVT Molecular Dynamics simulation is run to heat the structure to 3000 K for 4 ps, creating disorder in the structure. The next step is to cool the structure over 6 ps to 300 K. The final disordered configuration is geometry optimized using DFTB to ensure bond distances and coordination numbers (CN) are close to the experimental values, the optimization proceeds until the forces are below 0.05 eV Å$^{-1}$. The final structure is assessed by
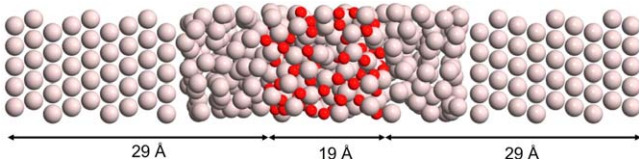
**Figure 1.** Illustration of the Al/AlOx/Al Junction Model.

analysing Al–O coordination number and radial distribution function to ensure the oxide is truly amorphous. The radial distribution function is calculated using equation (1).

$$g(r) = \frac{1}{4\pi r^2} \frac{1}{N\rho} \sum_{i=1}^{N} \sum_{j \neq i} \langle \delta(r - |r_i - r_j|) \rangle. \quad (1)$$

The junction is created by sandwiching the amorphous oxide between two $5 \times 5 \times 1$ layers of bulk Al (111), the structure is optimized using DFTB once again, to describe the bonding at the interface. This optimization creates disorder to the Aluminium layers at the surface as described in other studies before returning to the bulk Al structure [21, 23, 24]. The final junction structure for all our models have a oxide barrier length of 18–19 Å, which is within the experimental range of 10–20 Å [25]. Due to computational cost, the lateral dimensions of our junctions are considerably smaller than the experimentally fabricated JJ's for qubits applications. Hence, periodic boundary conditions are applied in the $x$, $y$ directions for the simulation. A typical Junction model in this work is illustrated in figure 1.

### 2.3. Transport calculation with DFTB/NEGF method

The charge transport through the junction is calculated by combining DFTB (for the electronic structure) with NEGF method. The NEGF formalism is a numerical method that gives a single-particle description of an electron moving through a potential. It has been successfully used to calculate the transport properties of a wide range of nanoscale devices such as molecular junctions, silicon nanowires, graphene systems, magnetic tunnel junctions and JJ [26–30]. A considerable advantage of this method is it allows the computation of transmission probability, charge density, current, local bond contribution to current and how they relate to the electronic structure of the system. By combining this methodology with the atomistic description of DFTB provides a powerful tool for exploring the atomic structure effects on the transport of the Al–AlOx–Al junction.

In this section we will provide a brief introduction to the NEGF formalism and the relevant equations as is implemented in the Quantum ATK software [31]. For a more comprehensive description of the method, readers are directed to some very good reviews in the literature [32–34].

The device is modelled into 3 sections, the left and right bulk electrodes described by conventional electronic structure calculation, and a central region where there is a non-equilibrium electron distribution. The system is treated with open boundary conditions in the transport direction, thus the left and right bulk electrodes are essentially semi-infinite leads. As the chemical potential will be different in the two

electrodes (when not under bias). The electron density from the left and right contributions are calculated separately.

$$n^{L/R} = \sum_{\alpha} |\psi_{\alpha}(r)|^2 f\left(\frac{\epsilon_{\alpha} - \mu_{L/R}}{k_b T}\right), \quad (2)$$

where $L/R$ refer to left and right regions, $\psi_a$ are the scattering states, f corresponds to a fermi function. $\epsilon$ is the electron energy, $\mu$ is the chemical potential of the electrode, $k_b$ is the boltzmann constant and $T$ is the temperature. Where the electron density is effectively the sum of the occupied scattering states.

Similarly the left/right density matrix contribution is calculated,

$$D^{L/R} = \int \rho^{L/R}(\epsilon) f\left(\frac{\epsilon_{\alpha} - \mu_{L/R}}{k_b T}\right) d\epsilon, \quad (3)$$

where $\rho^L$ is the spectral density matrix given by

$$\rho^L(\epsilon) \equiv \frac{1}{2\pi} G(\epsilon) \Gamma^L(\epsilon) G^{\dagger}(\epsilon), \quad (4)$$

$G$ is the retarded Green's function and $\Gamma$ is the broadening function of the electrodes, given in terms of self energies.

$$\Gamma^{L/R} = \frac{1}{i}\left(\left(\sum^{L/R}\right) - \left(\sum^{L/R^{\dagger}}\right)\right). \quad (5)$$

The key quantity to be calculated is the retarded Green's function calculated for the central region using the Hamiltonian of the central region and adding the self energies, $\sum$.

$$G(\epsilon) = \frac{1}{(\epsilon + i\delta_+)S - H - \sum^L(\epsilon) - \sum^{R(\epsilon)}}, \quad (6)$$

where $\delta_+$ is a infitesimal positive number, $S$ is the overlap matrix and $H$ is the hamiltonian matrix for the system, $\sum^{L/R}(\epsilon)$ are the self-energies. In Quantum ATK, the calculation of the Green's function at a specific energy is done by inversion of the Hamiltonian Matrix using an O(N) algorithm [35].

Once the non equilibrium density matrix has been obtained self consistently, the transmission probability for electrons of energy, $\epsilon$, can be obtained from the retarded Greens function by

$$T(\epsilon) = Tr[G(\epsilon)\Gamma^L(\epsilon)G^{\dagger}(\epsilon)\Gamma^R(\epsilon)]. \quad (7)$$

Once the $T(\epsilon)$ has been calculated from the retarded Green's function, the current can be straightforwardly computed using the Landauer–Buttiker formula [36].

$$I = \frac{2e^2}{h} \int T(\epsilon)[f_L(\epsilon) - f_R(\epsilon)]d\epsilon, \quad (8)$$

where $T(\epsilon)$ is the transmission coefficient, $f_{L/R}(E)$ are the Fermi functions of the electrodes, $e$ is the electron charge and $h$ is Planck's constant.

To calculate resistance of the junction, first the zero bias conductance of the system is computed as given by equation (9).

$$G = -\frac{2e^2}{h} \int T(\epsilon)\frac{\delta f_0(\epsilon)}{\delta\epsilon}d\epsilon, \quad (9)$$

where $f_0$ is the equilibrium Fermi–Dirac distribution function. The resistance is then simply:

$$R_N = \frac{1}{G}. \qquad (10)$$

The resistances under normal state of the junctions is a key parameter for estimating the critical current from the Ambegaokar–Baratoff equation [37].

$$I_c R_n = \frac{\pi \Delta}{2e} \tanh\left(\frac{\Delta}{2K_b T}\right), \qquad (11)$$

where $I_c$ is the critical current, $R_n$ is the normal state resistance, $\Delta$ is the superconducting parameter, which is taken as 190 $\mu$V at 100 mK [38].

### 2.4. Computational details

All calculations are carried out using the QuantumATK-2021 software [31]. The NVT Molecular Dynamics simulations are calculated using classical force fields. The 'ReaxFF' parameter set was chosen as it shows the limiting behaviour of oxidation in other studies and a good qualitative description of amorphous AlOx [24, 39].The electronic structure of all Junction models were calculated with DFTB using the 'magsil-1-1' parameter set [40–42]. A Monckhorst-Pack grid k-point sampling of $5 \times 5 \times 300$ is used whilst the density mesh cut off is set to 50 Hartree. The zero bias transmission is calculated with $9 \times 9$ k-point sampling grid as is the Projected Local Density of States (PLDOS) to analyze the electronic structure of the junction device. The junctions are studied under applied bias of $-1$ to 1 V, to simulate the current–voltage ($IV$) characteristics in normal state conduction (i.e not superconducting). All transport calculations are done at a temperature of 0 K.

## 3. Results and discussion

### 3.1. Creating the junction models

A typical junction model in this study is illustrated in figure 1. It is important to validate our amorphous models by ensuring they are in fact amorphous. This is achieved by comparing the radial distribution with that of crystalline corundum. In crystalline corundum there is clear long range and short range order shown by clear peaks as seen in figure 2. For amorphous AlOx, short range order is expected with a clear peak $\approx 1.8$–2 Å, accounting for the Al–O bond distance, but there should be no distinctive peaks at larger distances (no long range order) [22, 43]. This shows that the models created by the simulated annealing method are clearly amorphous. In addition, there are no peaks below 1.8 Å, confirming that there are no unrealistically short Al–O bonds within the barrier. All our junction models reported in this work show similar radial distribution plots as the one in figure 2.

Our aim in this work is to assess how the stoichiometry affects the atomic structure, and in turn strongly affects the
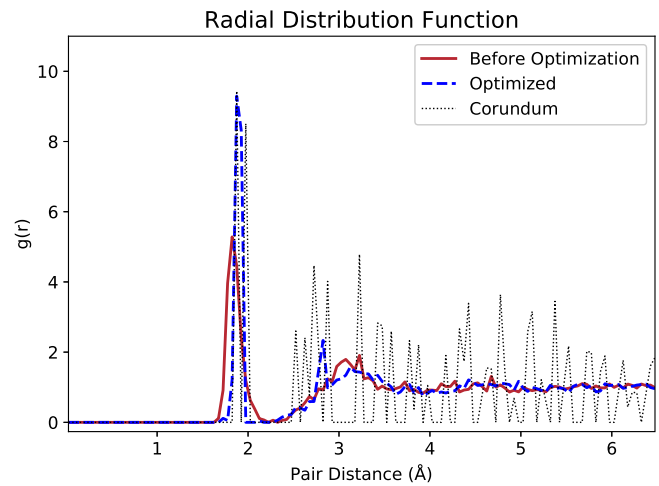


**Figure 2.** Radial Distribution comparing Corundum (Crystalline Al$_2$O$_3$), amorphous Al$_2$O$_3$ before and after optimization.

charge transport properties. However, Al:O ratio doesn't give any insight into the actual structure of the barriers. A quantitative way of understanding and comparing the differences between barriers is to analyse the Al–O coordination number. This measure gives an insight into the relative metallicity of the barriers in addition to the amorphous nature. Typical corundum would have no distribution of CN with all values being 6. In amorphous AlOx a distribution is expected, with higher number of highly coordinated Al expected for higher stoichiometries. The simulated annealing method is an approximate method that has been shown to give good qualitative amorphous structures. It can give unrealistic structures, which we try to circumvent by observing any unreasonable Al–O bond distances and coordinations. This is why the geometry optimization step after the annealing, carried out with DFTB, is key to ensure realistic barriers. The importance of this step is highlighted in figure 3 which shows the CN distribution before optimization, after optimization and after junction formation for a barrier with AlO$_{1.1}$ stoichioimetry.

As evident from figure 3 the geometry optimization improves the distribution across 2, 3, 4, 5 coordinated Al, namely the increase in 5 coordination, as ideally Al aims to be coordinated to 6 oxygens. This wider distribution illustrates a fixing of bond distances. This can also be seen in figure 2, where the peak at $\approx 1.9$ Å is much bigger after optimization. The coordination number distribution for all our models is in good agreement with experiment and other theoretical studies reported previously [21, 44, 45].

Figure 3, also shows the typical changes expected when the barrier is created into the junction. The distribution of 1 and 2 coordinated Al increases significantly as the barrier bonds to the surface Aluminium. Low coordinated Al is at the interface is typical which influences the effective stoichiometry and barrier length, one of the main sources of variability in Al/AlOx/Al. Hence, importantly replicated in our models.
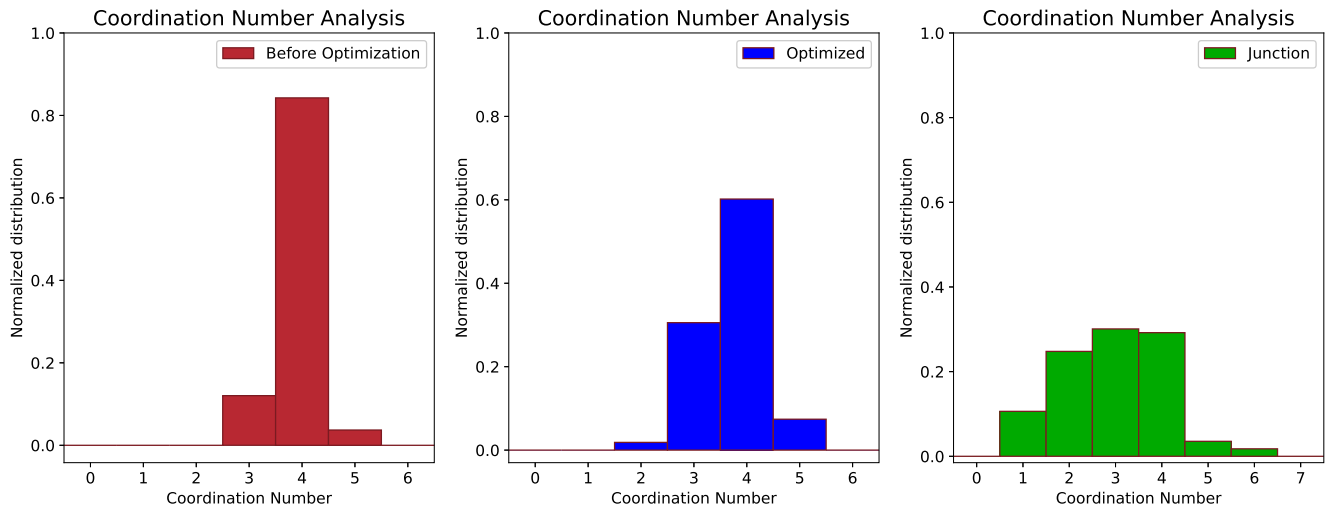
**Figure 3.** Comparison of atomic structure and the importance of optimization steps in junction creation.

## 3.2. Studying the influence of oxide stoichiometry on current-voltage characteristics of JJ's

In this section, the transport simulations with NEGF are reported and compared across stoichioimetry of 0.8 to 1.5. The zero bias transmission spectra and PLDOS was calculated for all junction models. The PLDOS highlights the electronic structure in the junction, specifically the metallicity of the barrier as oxygen concentration increases.

The electronic structure of amorphous $AlO_x$ and thin barriers in general is poorly understood and subject to debate. Unlike crystalline $AlO_x$ with a clear bandstructure and an accepted bandgap of around 9 eV, the 'bandgap' of amorphous $AlO_x$ is not so clear and is dependent on a variety of factors like structure, density, oxygen stoichiometry, fabrication method [46]. Several experimental studies have shown that amorphous $AlO_x$ structures have a significantly reduced 'bandgap' of between 2.8 and 3.2 eV [47–49]. The bandgap calculated here for the fully stoichiometric amorphous aluminium oxide lies between 2.3 and 3 eV, in good agreement with experiment.

The PLDOS highlights the electronic structure of the device as a function of the $Z$ coordinate (the transport direction). For our junction models, the barrier lies approximately between 20–25 Å and 40–45 Å. The PLDOS shown in figure 4 is a good gauge of metallicity of the insulating barrier, where continuous DOS in the region indicates metallic character. Our results show, as expected, that bandgaps only appear with increased stoichiometry. The DFT study by Kim *et al* report that bandgaps only open up for highly coordinated Al(CN $\geqslant$ 4) [23]. This is consistent with the results reported here, as higher stoichiometries have a much higher distribution of highly coordinated Al and hence gaps open up in the barrier as observed.

The electronic structure of the barrier plays a significant role in the expected transport of the entire junction. The $AlO_{0.8}$, $AlO_{1.1}$ barriers have continuous density of states in the barrier, so can be expected to be metallic in nature. It is evident, particularly below the Fermi level that gaps are
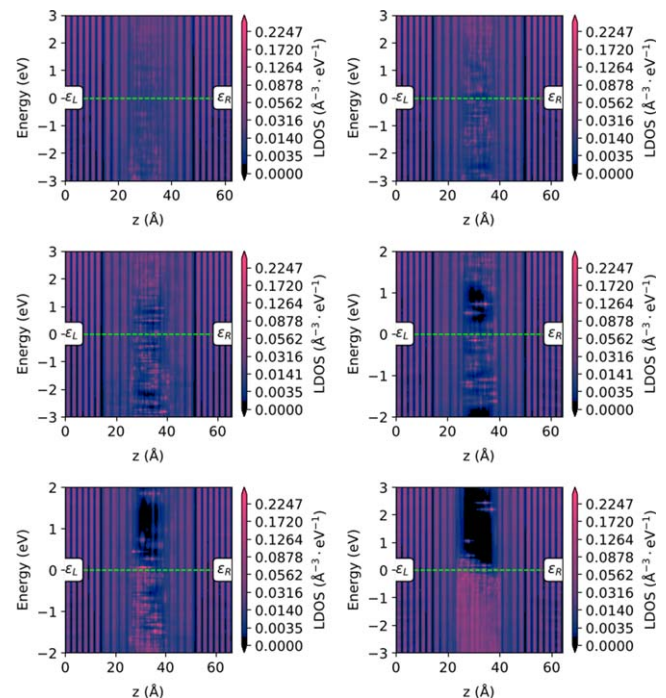


**Figure 4.** PLDOS for the different oxide stoichioimetry; Top left = 0.8, Top right = 1.1, centre left = 1.2, centre right = 1.3, bottom left = 1.4, bottom right = 1.5.

appearing for the $AlO_{1.2}$ barrier. The $AlO_{1.3}$ shows a more prominent gap above the Fermi level albeit with resonances disrupting the gap. Finally $AlO_{1.4}$ and fully stoichiometric $AlO_{1.5}$, show clear bandgaps due to highly coordinated Al. From these structures, it would be expected that with increased Al:O ratio, there would be significant increase of junction resistance.

In addition to the electronic structure, Al:O ratio has a significant influence on the atomic structure of the barrier as shown in figure 5. Generally, low stoichiometries (0.8, 1.1) lead to low distribution of 5 and 6 coordinated Al. There is a high distribution of 1, 2 and 3 coordinated Al, due to oxygen deficiency, this would be prevalent throughout the barrier and
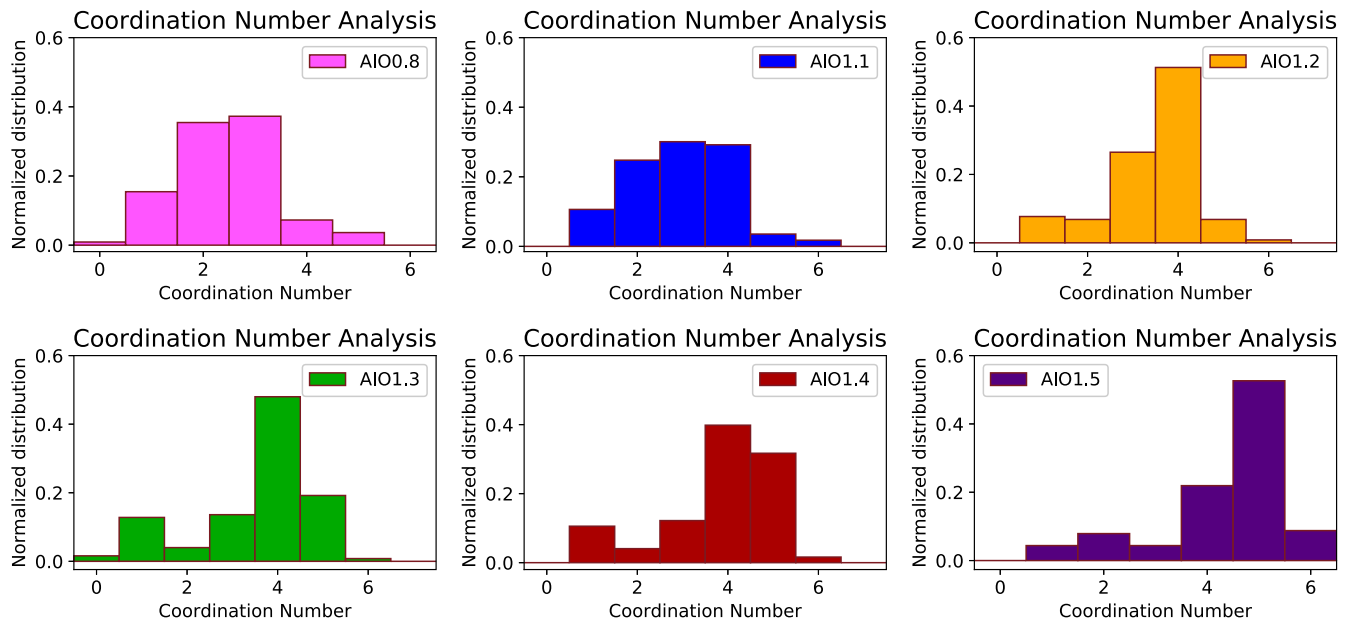
**Figure 5.** Coordination number analysis to quantify difference in atomic structure across different AlOx stoichiometries.

not just at the Al–AlOx interface. Increase in oxygen content increases significantly the distribution of the four coordinated aluminium, whilst reducing the low coordinated Al. There is also a clear increase of 5 coordinated Al which becomes more abundant until it dominates in fully stoichiometric barriers.

As a next step we have evaluated the current flow through the junctions reported above. All our models were studied under applied bias ($-1$ V to 1 V) and the *IV* characteristics computed shown in figures 6 and 7. Due to the comparatively (to experiment) small size of the junctions, qualitative comparison is appropriate. Though, microAmp currents are reasonable and the *IV* characteristic is typical of that of a Josephson Junction (linear at low bias), suggesting the essential physics is being captured by the chosen simulation methods. Figure 6 shows the *IV* curves for stoichiometries ranging from 0.8 to 1.5. As expected from the discussion on atomic and electronic structure, the current is significantly higher for $AlO_{0.8}$ than for the other barriers. The barrier is significantly metallic in nature therefore has a much higher conductance, with currents more than 2 times that of $AlO_{1.1}$. In order to more easily compare the junctions 1.1–1.5, figure 7 shows the *IV* curves without the $AlO_{0.8}$ structure.

The *IV* characteristics follow the predicted trend of higher Al:O resulting in lower current, with only slight deviations. Firstly, $AlO_{1.1}$ barrier is significantly more conducting than the rest, with currents 3–4 times larger. This is consistent with the analysis of the electronic structure and PLDOS as there are no gaps seen around the Fermi level. As a result, the barrier behaves more metallic and as expected is more conductive.

The rest of the junctions show slight differences in the magnitude of current. Surprisingly $AlO_{1.3}$ is more conducting than $AlO_{1.2}$ in the positive bias regime, and they have similar currents in the negative bias regime. From the electronic structure, it may be expected that $AlO_{1.3}$ would show more resistance, due to the clearer bandgap. However, analysis of

the atomic structure in the barrier, it can be seen that $AlO_{1.2}$ shows a higher 4 coordinated distribution and a lower 1 and 2 coordinated Al than expected for this stoichiometry. As a result, the barrier may be more insulating than expected. Hence, it shows similar characteristics to $AlO_{1.3}$. This example illustrates why Al:O ratio alone is not a good metric for understanding differences in junction performance, in fact it is the local atomic structure, better described by the coordination number that gives insight into how the atomic structure affects performance.

It is also important to note that another barrier, also $AlO_{1.3}$, could have a different local atomic structure and thus different device performance. This is discussed in detail in the next section for $AlO_{1.1}$ barriers. Lastly, figure 7 shows that the fully stochiometric barrier has significantly lower currents (nA range) than the rest of the barriers. This is easily explained through much higher distribution of highly coordinated Al as well as a clear bandgap in the PLDOS. Though the PLDOS at zero bias shows the gap formation above the Fermi level, under bias, the resonances shift and this gap is firmly within the bias window, consequently affecting the *IV* curves. This is illustrated at the bottom part of in figure 8. As a result, this barrier would be more insulating and hence have higher resistance/produce lower currents.

In addition to the *IV* characteristics, we compute the resistance*area (RA) product as it is how the Junction resistance is commonly reported experimentally. Normal state resistance is an important junction parameter as using the Ambegaokar–Baratoff relation, it allows us to estimate the critical current of the device when it is superconducting. Control of the critical current $I_c$ is key for the fabrication of high quality qubits. By studying how the resistance of junctions varies, we can probe the superconducting properties and how they relate to the atomic structure of the junction. Figure 9 shows how the RA varies with stoichiometry from our simulated junctions. The $AlO_{1.5}$ model has been excluded
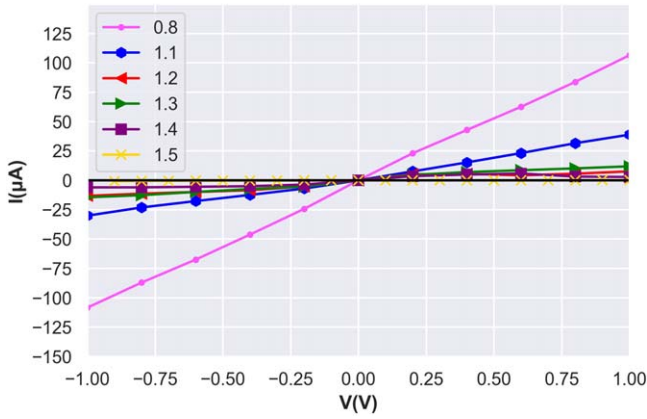
**Figure 6.** Current–voltage (*I–V*) curves for different oxide stoichiometries (0.8–1.5).
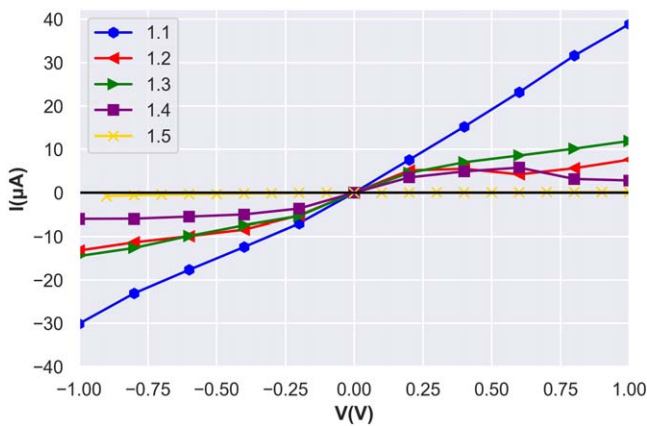


**Figure 7.** Current–voltage (*I–V*) curves for different oxide stoichiometries (excluding 0.8).

for clarity as its RA is two orders of magnitude higher. This way we can more reasonably compare how RA changes between 0.8 and 1.4. The RA values are also reported along with the computed critical current density, $J_c$, in table 1. The simulated values of RA are underestimated compared to experimentally observed junctions. Our junctions have RA in the range of $1 \, m\Omega \, \mu m^2$–$10 \, \Omega \, \mu m^2$ compared to the experimentally expected range of $250 \, \Omega \, \mu m^2$–$25 \, k\Omega \, \mu m^2$. This is expected for a variety of reasons. Firstly, the size of our junctions cannot meet the experimental range, the cross sectional area of the junctions are $\approx 1.4 \, nm \times 1.4 \, nm$ whereas for experimental junctions are typically $\approx 100 \, nm \times 100 \, nm$. Although periodic boundary conditions are applied, this is still an approximation to artificially increase the size of the junction, though cannot fully account for effects of junction size and so the resistance is underestimated. Secondly, these model junctions represent the most ideal structure with no impurities, no effects from measurement techniques and no discernible defects. As a result the resistance can be expected to be underestimated. However, a qualitative comparison between the models is still valid, which allows us to explore the atomistic effects on the electrical response of the junctions.

The variation of RA with stoichiometry is consistent with the computed *IV* curves. The RA for $AlO_{0.8}$ and $AlO_{1.1}$ is the lowest and close in value. There is a significant increase in RA of $AlO_{1.2}$ of more than three times the RA of $AlO_{1.1}$. The anomaly of $AlO_{1.2}$ producing less current than $AlO_{1.3}$ is supported here by the drop in RA for the $AlO_{1.3}$ barrier of more than $1 \, m\Omega \, \mu m^2$. As discussed above, this is due to a highly coordinated barrier for $AlO_{1.2}$ leading to a more insulating gap than expected. Finally $AlO_{1.4}$ has a RA more than 8 times that of $AlO_{0.8}$, as seen from table 1 $AlO_{1.5}$ is even bigger with RA $\approx 7 \, \Omega \, \mu m^2$. These results show a clear but complex relationship between Al:O ratio and junction resistance, where increased oxygen content leads to significant increases in the resistance. Though Al:O alone cannot be relied on, as local atomic structure can strongly influence the 'effective stoichiometry' of the barrier and lead to larger than expected resistances as seen in $AlO_{1.2}$.

In the work by Cyster and co workers, they also explore the effect of stoichiometry on Al/AlOx/Al models using NEGF [17]. They report RA values that range between $10^{-2}$ and $10^3 \, \Omega \, \mu m^2$, a similar range to what we have calculated here. They also find considerable increases in resistance with increasing oxygen content. They report a transition from metallic to insulating at stoichiometries of 0.9, we observe a similar transition at $\approx 1.1$, the difference is most likely due to the local atomic structure of the oxide barrier, emphasising that this is a better measure than Al:O ratio. Direct comparison between their reported RA values and our results, is difficult due to different electronic structure models employed and Cyster and co workers models have an oxide barrier length of $14 \, \text{Å}$, whereas our models are $19 \, \text{Å}$. Cyster and co workers show a drop of resistance at higher stoichiometries, which they attribute to the oxygen distribution within the barrier. Our results predict a continued increase in resistance with increasing oxygen content with no similar drop. These discrepancies highlight the sensitivity of the local Al–O structure on the electrical response, compared to the Al:O ratio itself.

The critical current density has been computed by dividing the critical current computed from equation (5) by the cross sectional area of the junction, these are shown in table 1. As the resistances have been underestimated, it can be expected that the critical currents for our models are overestimated. Experimentally, high quality Al JJs for qubit applications can expect a critical current density, $J_c$, of $1$–$10^3 \, A \, cm^{-2}$, whereas our model junctions range from 1 to $10^6 \, A \, cm^{-2}$. Our simulations show that the $J_c$ is sensitive to the atomic structure of the barrier and not just the Al:O ratio, density, barrier length, junction size, hence the difficulty in consistent reproducible junctions. Controlling the barrier structure, either by epitaxial growth, or otherwise should lead to more favourable control of critical current.
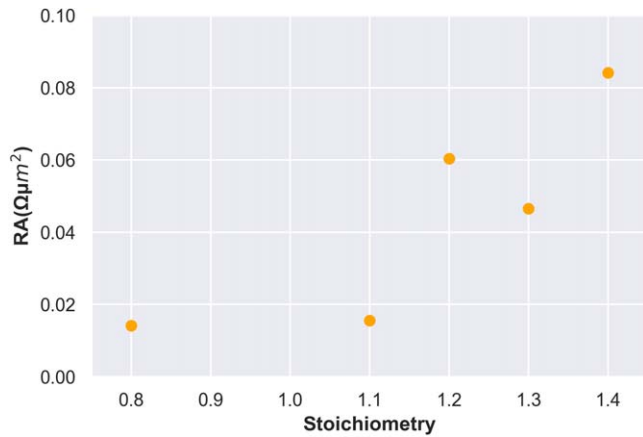
### 3.3. Variability of Al/AlOx/Al junctions

A main challenge in using Josephson Junction devices in qubit circuits is the lack of control of the critical current of the junction. Due to the amorphous nature of the barrier there is
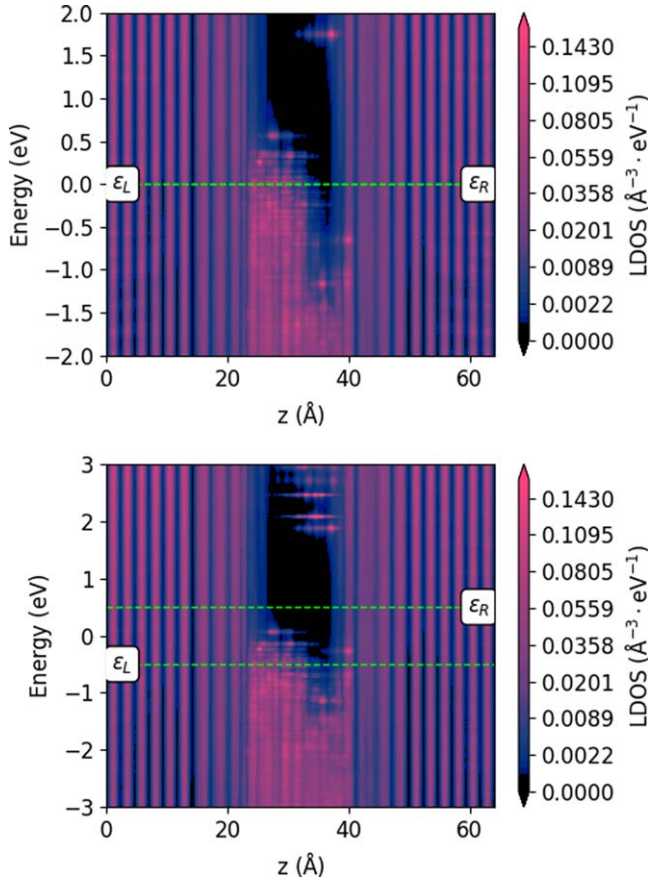
**Figure 8.** PLDOS of $AlO_{1.5}$ barriers at zero bias (top) and a bias of 1 V (below).



**Figure 9.** RA versus stoichiometry.

**Table 1.** Calculated resistance-area values (RA) and critical current density for the different AlOx stoichiometries.

| Stoichiometry | RA ($\Omega\ \mu m^2$) | $J_c$ (A cm$^{-2}$) |
| --- | --- | --- |
| 1.5 | 6.948 | $4.28 \times 10^3$ |
| 1.4 | 0.084 | $3.54 \times 10^5$ |
| 1.3 | 0.046 | $6.41 \times 10^5$ |
| 1.2 | 0.060 | $4.93 \times 10^5$ |
| 1.1 | 0.016 | $1.91 \times 10^6$ |
| 0.8 | 0.014 | $2.10 \times 10^6$ |

often significant variability in the critical current values from junction to junction even if they are fabricated in the same wafer. In this section of the paper, our aim is to simulate multiple junction models where all device and material parameters are kept the same in order to replicate the variability in the critical current. Additionally, we aim to understand how this variability arises in order to help overcome it and guide the fabrication process.
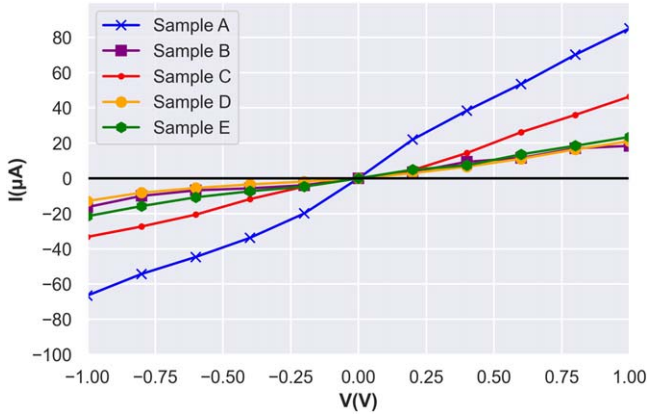
We report here 5 different $Al/AlO_{1.1}/Al$ junctions, all generated the same way as described above. The $AlO_{1.1}$ stoichiometry was chosen as it is suggested by literature and experimental data to be the most common stoichiometry from most junction material growth processes.

Figure 10 shows the *IV* characteristics for 5 different $Al/AlO_{1.1}/Al$ samples. All junctions qualitatively replicate the expected *IV* curve of a typical Josephson Junction. As is evident, there is variability across the devices. In particular sample A is the most conductive, with currents 2–4 times that of the other samples. Sample C is more conductive by 1.5–2 times that of B, D and E. Whilst samples B, D, E show remarkable consistency, with almost inseparable *IV* curves. Figure 11 reports the variation in RA across the 5 samples. The RA values range from 0.016 to 0.156 $\Omega\ \mu m^2$. These are also reported along with the critical current densities in table 2. Sample A has the lowest RA, which is consistent with the *IV* curve in figure 10, sample D appears to have the lowest current and hence the fact it has the highest RA is expected.

The calculated critical current densities are in the range of $10^5–10^6$ $A\ cm^{-2}$. The differences between samples follow the inverse of the RA trend, as expected as the critical current is calculated from the resistance values. Excluding Sample A, the values for B, C, D, E are all within the same order of magnitude, and are close in value though clear variability remains. This is similar to the results reported by Kim *et al*, in their DFT study of Al/AlOx/Al barriers they find variability in the computed critical current density even when the stoichiometry and length of the barriers are similar [23]. Specifically, Kim *et al* report that for two barriers with a mean thickness of 7.1–7.2 Å the critical current varies by factor of more than 2.6. The variation in our samples (B, C, D, E) ranges by a factor between 1.8 and 2.8.

In all cases the density, barrier length, oxide stoichiometry and preparation method are all the same, yet differences in resistance and transport remain. Sample A produces the highest current in normal conduction, has the lowest calculated RA and its superconducting critical current is an order of magnitude higher than the other samples. This can be explained by contrasting the atomic structure through the distribution of Aluminium coordination number as reported in figure 12.

The low resistance of sample A is consistent with the high distribution of low coordinated Al (CN = 1, 2, 3) compared to the other samples. Equally, there is a lower distribution of highly coordinated Al (CN = 4, 5, 6). As a result, the barrier would be expected to be more metallic. Hence more conductive, as predicted. The distribution of coordination number (CN) for samples B–D are very similar with only subtle differences.
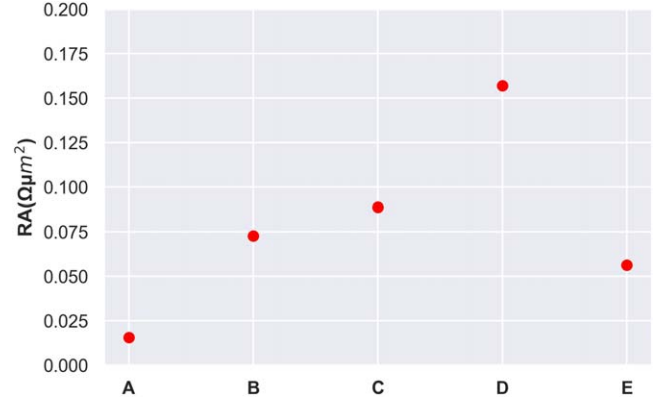
**Figure 10.** Comparison of the *IV* curves 5 different AlO$_{1.1}$ junction samples.



**Figure 11.** RA comparison across the five different samples.

**Table 2.** Calculated resistance-area values (RA) and critical current density for the different Junction Samples.

| Junction | RA ($\Omega$ $\mu$m$^2$) | $J_c$ (A cm$^{-2}$) |
|---|---|---|
| Sample A | 0.016 | $1.91 \times 10^6$ |
| Sample B | 0.072 | $4.11 \times 10^5$ |
| Sample C | 0.087 | $3.43 \times 10^5$ |
| Sample D | 0.156 | $1.90 \times 10^5$ |
| Sample E | 0.056 | $5.30 \times 10^5$ |

In addition to local atomic strucure, it is important to compare the electronic structure of the junctions for understanding differences. Comparing the PLDOS of samples B, D, E in figure 13 it can be seen that for sample D, there is an opening of a small energy gap just above the Fermi level. This leads to a break in the metallicity of the barrier and helps explain why the RA for this junction is higher than the others. This gap may arise due to a higher distribution in highly coordinated Al, particularly Al(3). Once more demonstrating that small differences in the structure of the amorphous barrier can lead to significant variability in performance of the junctions.

Despite the atomic structure of B, C, D and E being only subtly different, the *IV* characteristics show C produces more current than B, D and E. Variability structure to structure is emphasised by the transmission spectra which shows the different energies (relative to the Fermi level) at which the electrons can scatter through the device, and the relative probability (($T$)($E$)) of the electron being transmitted. The area under the curve gives the conductance of the device system.

The transmission spectra at zero bias is shown in figure 14, only peaks between the energies of −0.5 to 0.5 eV are shown as these are the only ones relevant within the −1 and 1 V bias range. Under bias the peaks will change slightly in intensity and can shift further apart. However, the zero bias spectra gives good insight to the conductance of the junction. Samples B and C have a thicker linewidth for easier comparison. The intensity (given by T(E)) for the different samples is consistent with the *IV* characteristics shown in figure 10.

The peaks in the transmission spectra relate to conduction pathways through the oxide barrier. These conduction pathways depend on the local atomic structure of the barrier. As seen from the spectra, despite the density, stoichiometry, length and material type all being identical, the amorphous nature of the barrier leads to significant variability in electronic structure, resistance and charge transport. The sensitivity to atomic structure is a challenge for consistent

fabrication of Al/AlOx/Al and other JJ's for controlling the $I_c$ and reducing decoherence in superconducting qubits.

### 3.4. Analysis of transmission pathways

Tunnelling through the oxide is hypothesized to occur through metallic pathways. It has been suggested that oxygen deficiency increases the metallic pathways within the oxide and thus increases the conductance across the barrier. It can also lead to leakage of cooper pairs, leading to increased noise and decoherence in superconducting qubits. As discussed above, the peaks in the transmission spectra correspond to transmission pathways in the device. The transmission coefficient at specific energies can be split into local bond contributions, as described by equation (12) [50, 51].

$$T(E) = \sum_{i \in A, j \in B} T_{ij}(E). \tag{12}$$

The local bond contributions can be visualised in the barrier, and can show positive pathways *i* to *j* or negative *j* to *i* (back scattering). Predicting this flow of electrons can give further insight to how the amorphous nature of the barrier influences the properties of the junction.

Analysis has been carried out on all AlO$_{1.1}$ junctions, only peaks within the applied bias range were examined. Here, we report on sample B. Figure 15 shows the transmission spectra for sample B with the relevant peaks highlighted by the dotted box. The transmission peaks in this region show the most prevalent conduction pathways in the barrier. Figure 16 illustrates the visualisation of the conduction pathway at 0.03 eV for sample B, very close to the Fermi
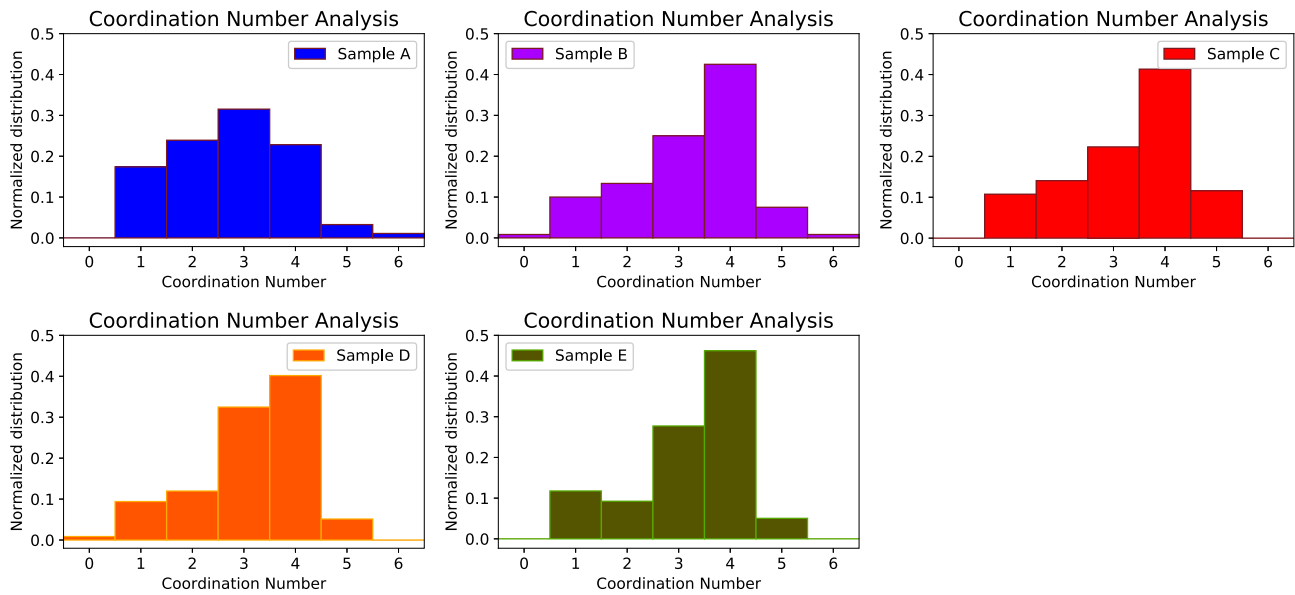
**Figure 12.** Coordination number analysis across 5 samples of $Al/AlO_{1.1}/Al$.

level. Only bond contributions higher than 20% of the T(E) at that peak is shown.

From the pathway in figure 16, it can be seen that predominantly electrons flow from Al to Al, consistent with the transport being dominated by metallic conduction pathways. The transmission of electrons doesn't necessarily flow between directly bonded Al atoms, therefore longer range tunneling occurs. From this pathway, several 'routes' can be identified. There is a group of Al atoms that contribute the highest weight to T(E) (highlighted by the purple arrows) this group identifies a 'hotspot' within the barrier. This is consistent with the findings in [17] which report 'hotspots' corresponding to metallic conduction pathways. Finally, it can also be seen some arrows travelling in the opposite direction, which shows back scattering, which would decrease the conductance and hence can give an insight to rises in resistance within the barrier.

Further analysis of the transmission pathways in sample B found similar results. Namely, transmission is dominated by metallic pathways Al to Al. Peaks at 0.21 eV, −0.03 eV, all contain, in addition to others, the same atoms as those that dominate the pathway in 0.03 eV, this highlights the strong influence of local atomic structure, that creates 'hotspots' which contribute to the conductance at various different energies. Although, there are examples of Al–O bond contributions to the transmission, transport through the oxygen atoms is much less common, and suggests increasing oxygen concentration increases the resistance (decreases the $I_c$) of the junction.
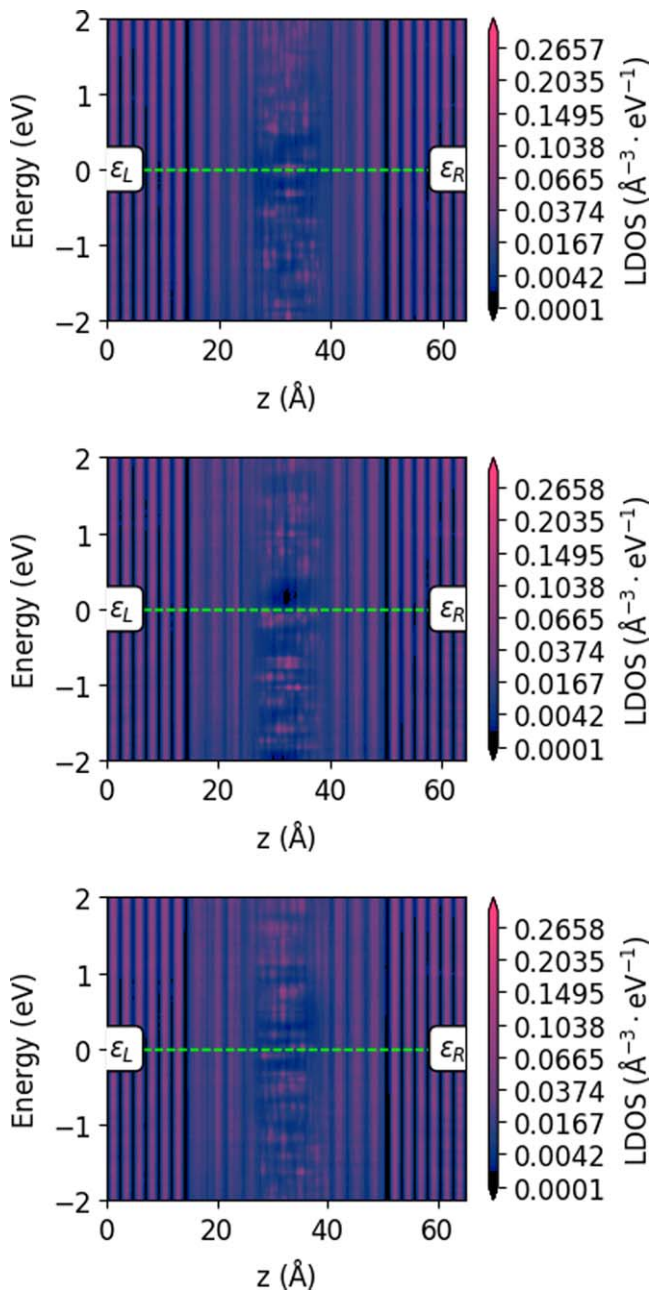
Lastly, from analysis of pathways through other junctions, it was found that the transmission at different peaks, had common atoms in the dominant pathways, hence 'hotspot' areas in the amorphous barrier. The pathways are also dominated by Al–Al contributions, including long range order, suggesting metallic pathways through the barrier are key to transport in the junction. Additional transport pathways can be found in the supporting information.

## 4. Conclusions

Atomistic understanding of Al/AlOx/Al and other JJ is key to improving their fabrication process and achieving control of critical current and other parameters. Developing and employing efficient and accurate modelling techniques can significantly boost progress and understanding of the Al/ AlOx/Al. In this work we have thoroughly studied the atomic and electronic structure of the archetypal Josephson Junction Al/AlOx/Al and explored how it affects junction performance, through a combination of molecular dynamics, DFTB and NEGF methods.
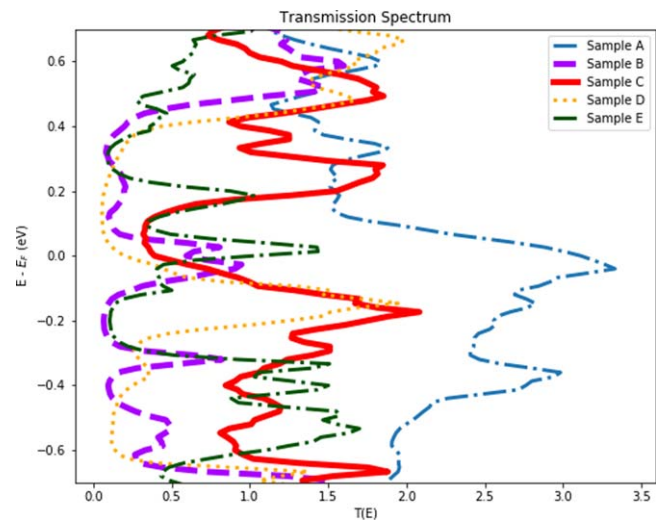
Through our calculations, it has been shown that the stoichiometry of the barrier sensitively affects the critical current of the Al/AlOx/Al, the effects can be rationalised through the opening of a energy gap in the barrier with increasing oxygen concentration, linked to the local atomic structure studied by Al–O coordination number. The amorphous nature of the barrier leads to unavoidable variability within the junction, this has been studied here computationally across different samples created in the same way. It was found that differences in local structure arise naturally which strongly influences the electronic structure of the barrier leading to variability in the *IV* characteristics, junction resistance and critical currents. Though some consistency between samples was observed, small differences in structure resulted in significant variation in the simulated current values and hence the device performance. Though not explored in this paper, further work could focus on the specific sources of variability and whether the models can capture the natural defects that lead to decoherence in superconducting qubit circuits.

**Figure 14.** Transmission spectrum for the five different $AlO_{1.1}$ samples.



**Figure 15.** Sample B transmission spectra. Dotted box highlights the peaks associated with the *IV* curves.

computational framework, could explore the influence of barrier density, effective barrier length, crystalline junctions, different material junctions and crucially explore defects and sources of noise within the barriers.
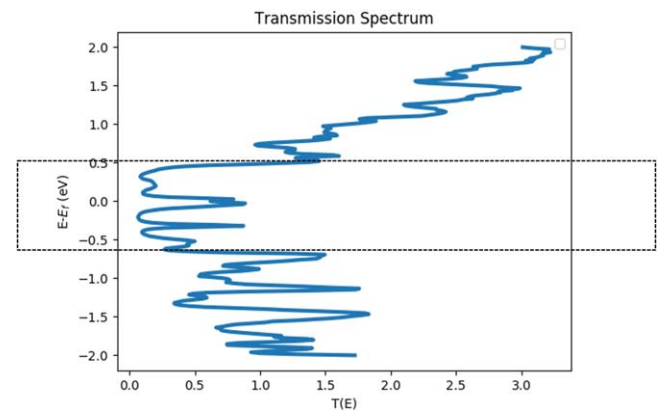


**Figure 13.** PLDOS comparison for sample B(top), D(middle), E(bottom).

Finally, within our computational framework we have explored the nature of tunnelling through the barrier. Analysis of the transmission pathways provides further evidence that metallic pathways dominate the transport in the junction. As a result, increased oxygen concentration (higher stoichiometry) reduces the metallic pathways in the barrier and lead to increased resistance. This is further evidence that local atomic structure is vitally important for controlling critical currents.

In conclusion, computational modelling using atomistic semi-empirical methods is an efficient tool to compliment experimental work in improving our understanding of JJ and accelerating the improved performance of superconducting qubits and other technology. Further work, using this

## 5. Additional information

Additional Transmission Pathways can be found in the supplementary information. All *x*, *y*, *z* coordinates for the model junctions are available on request.
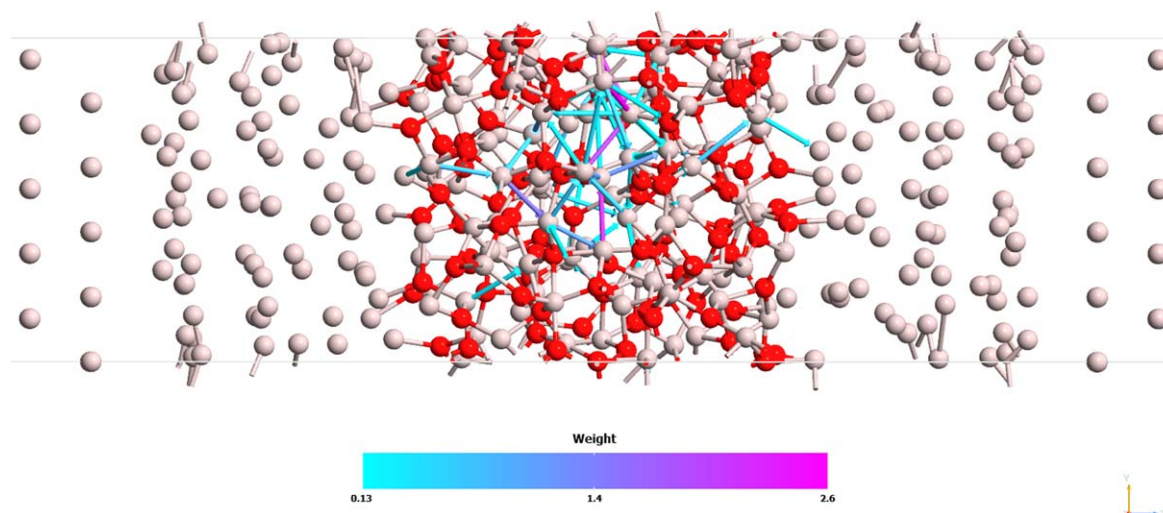
## Acknowledgments

**Figure 16.** Transmission pathway for the peak at 0.03 eV in the transmission spectra for Sample B.

## Data availability statement

The data that support the findings of this study are available upon reasonable request from the authors.

## ORCID iDs

Paul Lapham ⓘ https://orcid.org/0000-0001-8005-3564
Vihar P Georgiev ⓘ https://orcid.org/0000-0001-6473-2508

## References

[1] Clarke J and Wilhelm F K 2008 Superconducting quantum bits *Nature* **453** 1031–42

[2] Jaklevic R C, Lambe J, Silver A H and Mercereau J E 1964 Quantum interference effects in Josephson tunneling *Phys. Rev. Lett.* **12** 159–60

[3] Kjaergaard M, Schwartz M E, Braumüller J, Krantz P, Wang J I J, Gustavsson S and Oliver W D 2020 Superconducting qubits: current state of play *Annu. Rev. Condens. Matter Phys.* **11** 369–95

[4] Koch J, Yu T M, Gambetta J, Houck A A, Schuster D I, Majer J, Blais A, Devoret M H, Girvin S M and Schoelkopf R J 2007 Charge-insensitive qubit design derived from the Cooper pair box *Phys. Rev.* A **76** 1–19

[5] Müller C, Cole J H and Lisenfeld J 2019 Towards understanding two-level-systems in amorphous solids: insights from quantum circuits *Rep. Prog. Phys.* **82** 124501

[6] Krantz P, Kjaergaard M, Yan F, Orlando T P, Gustavsson S and Oliver W D 2019 A quantum engineer's guide to superconducting qubits *Appl. Phys. Rev.* **6** 1–66

[7] Martinis J M, Devoret M H and Clarke J 2020 Quantum Josephson junction circuits and the dawn of artificial atoms *Nat. Phys.* **16** 234–7

[8] Josephson B D 1974 The discovery of tunnelling supercurrents *Proc. IEEE* **62** 838–41

[9] Gosner J, Kubala B and Ankerhold J 2019 Quantum properties of a strongly driven Josephson junction *Phys. Rev.* B **99** 7–9

[10] Chen C, Zuo Y, Ye W, Li X, Deng Z and Ong S P 2020 A critical review of machine learning of energy materials *Adv. Energy Mater.* **10** 1–36

[11] Yang C, Kim Y, Ryu S and Gu G X 2019 Using convolutional neural networks to predict composite properties beyond the elastic limit *MRS Commun.* **9** 609–17

[12] Vogiatzis K D, Polynski M V, Kirkland J K, Townsend J, Hashemi A, Liu C and Pidko E A 2019 Computational approach to molecular catalysis by 3d transition metals: challenges and opportunities *Chem. Rev.* **119** 2453–523

[13] Bendova M, Pytlicek Z, Prasek J and Mozalev A 2019 The growth and unique electronic properties of the porous-alumina-assisted hafnium-oxide nanostructured films *Electrochim. Acta* **327** 135029

[14] He Y F, Chu D Y and Zhuo Z 2021 Cycle stability of dual-phase lithium titanate (lto)/TiO$_2$ nanowires as lithium battery anode *J. Multidiscip. Appl. Nat. Sci.* **1** 54–61

[15] Jahan N, Hussain S, Rahman H U, Manzoor I, Pandey S, Habib K, Ali S K, Pandita R and Upadhyay C 2021 Structural, morphological and elemental analysis of selectively etched and exfoliated Ti$_3$AlC$_2$ MAX phase *J. Multidiscip. Appl. Nat. Sci.* **1** 13–7

[16] Tan E, Mather P G, Perrella A C, Read J C and Buhrman R A 2005 Oxygen stoichiometry and instability in aluminum oxide tunnel barrier layers *Phys. Rev.* B **71** 161401

[17] Cyster M J, Smith J S, Vaitkus J A, Vogt N, Russo S P and Cole J H 2020 Effect of atomic structure on the electrical response of aluminum oxide tunnel junctions *Phys. Rev. Res.* **2** 013110

[18] Spiegelman F, Tarrat N, Cuny J, Dontot L, Posenitskiy E, Martí C, Simon A and Rapacioli M 2020 Density-functional tight-binding: basic concepts and applications to molecules and clusters *Adv. Phys.X* **5** 1710252

[19] Stokbro K, Petersen D E, Smidstrup S, Blom A, Ipsen M and Kaasbjerg K 2010 Semiempirical model for nanoscale device simulations *Phys. Rev.* B **82** 1–7

[20] Elstner G M, Porezag D, Jungnickel G, Elsner J, Haugk M, Frauenheim T, Suhai S and Seifert G 1998 Self-consistent-charge density-functional tight-binding method for simulations of complex materials properties *Phys. Rev.* B **58** 7260–8

[21] DuBois T C, Cyster M J, Opletal G, Russo S P and Cole J H 2016 Constructing ab initio models of ultra-thin Al-AlOx-Al barriers *Mol. Simul.* **42** 542–8

[22] Gutiérrez G and Johansson B 2002 Molecular dynamics study of structural properties of amorphous (formula presented) *Phys. Rev.* B **65** 1–9

[23] Kim C E, Ray K G and Lordi V 2020 A density-functional theory study of the Al/AlOx/Al tunnel junction *J. Appl. Phys.* **128** 155102

[24] Cyster M J, Smith J S, Vogt N, Opletal G, Russo S P and Cole J H 2021 Simulating the fabrication of aluminium oxide tunnel junctions *Npj Quantum Inf.* **7** Article Number: 12

[25] Zeng L J, Nik S, Greibe T, Krantz P, Wilson C M, Delsing P and Olsson E 2015 Direct observation of the thickness distribution of ultra thin AlOxbarriers in al/AlOx/ al josephson junctions *J. Phys. D: Appl. Phys.* **48** 395308

[26] Rallis K, Dimitrakis P, Karafyllidis I G, Rubio A and Sirakoulis G C 2021 Electronic properties of graphene nanoribbons with defects *IEEE Trans. Nanotechnol.* **20** 151–60

[27] Martinez A, Price A, Valin R, Aldegunde M and Barker J 2016 Impact of phonon scattering in Si/GaAs/InGaAs nanowires and FinFets: a NEGF perspective *J. Comput. Electron.* **15** 1130–47

[28] Shohany B G, Roknabadi M R and Kompany A 2018 DFT-NEGF simulation of graphene-graphdiyne-graphene resonant tunneling transistor *Comput. Mater. Sci.* **144** 280–4

[29] Clendennen C, Mori N and Tsuchiya H 2015 Non-equilibrium Green function simulations of graphene, silicene, and germanene nanoribbon field-effect transistors *J. Adv. Simul. Sci. Eng.* **2** 171–7

[30] Lapham P, Vilà-Nadal L, Cronin L and Georgiev V P 2021 Influence of the contact geometry and counterions on the current flow and charge transfer in polyoxometalate molecular junctions: A density functional theory study *J. Phys. Chem.* C **125** 3599–610

[31] Smidstrup S *et al* 2020 QuantumATK: An integrated platform of electronic and atomic-scale modelling tools *J. Phys. Condens. Matter* **32** 015901

[32] Maassen J, Harb M, Michaud-Rioux V, Zhu Y and Guo H 2013 Quantum transport modeling from first principles *Proc. IEEE* **101** 518–30

[33] O'Donnell R 2008 Modeling of nanoscale devices *Proc. IEEE* **96** 1509–10

[34] Datta S 2000 Nanoscale device modeling: the Green's function method *Superlattices Microstruct.* **28** 253–78

[35] Petersen D E, Sørensen H H B, Hansen P C, Skelboe S and Stokbro K 2008 Block tridiagonal matrix inversion and fast transmission calculations *J. Comput. Phys.* **227** 3174–90

[36] Datta S 2005 *Quantum Transport: Atom to Transistor* (New York: Cambridge Univ. Press)

[37] Ambegaokar V and Baratoff A 1963 Tunneling between superconductors *Phys. Rev. Lett.* **10** 486–9

[38] Weides M *et al* 2011 Phase qubits fabricated with trilayer junctions *Supercond. Sci. Technol.* **24** 055005

[39] Hong S and Van Duin A C T 2016 Atomistic-scale analysis of carbon coating and its effect on the oxidation of aluminum nanoparticles by ReaxFF-molecular dynamics simulations *J. Phys. Chem.* C **120** 9464–74

[40] Frenzel J, Oliveira A F, Jardillier N, Heine T and Seifert G 2009 Semi-relativistic, self-consistent charge Slater-Koster tables for density-functional based tight-binding (DFTB) for materials science simulations, TU-Dresden 2004–2009 (https://dftb.org/parameters/download/matsci/matsci-0-3-cc)

[41] Frenzel J, Oliveira A F, Duarte H A, Heine T and Seifert G 2005 Structural and electronic properties of bulk gibbsite and gibbsite surfaces *Z. Anorg. Allg. Chem.* **631** 1267–71

[42] Guimarães L, Enyashin A N, Frenzel J, Heine T, Duarte H A and Seifert G 2007 Imogolite nanotubes: stability, electronic, and mechanical properties *ACS Nano* **1** 362–8

[43] Ishizawa N, Miyata T, Minato I, Marumo F and Iwai S 1980 A structural investigation of $\alpha$-Al$_2$O$_3$ at 2170 K *Acta Crystallogr.* B **36** 228–30

[44] Lee S K, Lee S B, Park S Y, Yi Y S and Ahn C W 2009 Structure of amorphous aluminum oxide *Phys. Rev. Lett.* **103** 4–7

[45] Momida H, Nigo S, Kido G and Ohno T 2011 Effect of vacancy-type oxygen deficiency on electronic structure in amorphous alumina *Appl. Phys. Lett.* **98** 2–5

[46] Filatova E O and Konashuk A S 2015 Interpretation of the Changing the Band Gap of Al$_2$O$_3$ Depending on Its Crystalline Form: Connection with Different Local Symmetries *J. Phys. Chem.* C **119** 20755–61

[47] Costina I and Franchy R 2001 Band gap of amorphous and well-ordered Al$_2$O$_3$ on Ni3Al(100) *Appl. Phys. Lett.* **78** 4139–41

[48] Shi S, Qian S, Hou X, Mu J, He J and Chou X 2018 Structural and optical properties of amorphous Al$_2$O$_3$ thin film deposited by atomic layer deposition *Adv. Condens. Matter Phys.* **2018** 7598978

[49] Åhammar C *et al* 2011 Unveiling the complex electronic structure of amorphous metal oxides *Proc. Natl. Acad. Sci. USA* **108** 6355–60

[50] Behera S K, Bora M, Paul Chowdhury S S and Deb P 2019 Proximity effects in graphene and ferromagnetic CrBr$_3$ van der Waals heterostructures *Phys. Chem. Chem. Phys.* **21** 25788–96

[51] An Y, Jiao J, Hou Y, Wang H, Wu R, Liu C, Chen X, Wang T and Wang K 2019 Negative differential conductance effect and electrical anisotropy of 2D ZrB$_2$ monolayers *J. Phys. Condens. Matter* **31** 065301